DOI: 10.1002/((please add manuscript number))

Article type: Full Paper

Self-Catalyzed Growth of Co-N-C Nanobrushes for Efficient Rechargeable Zn-Air Batteries

Hao Luo, Wen-Jie Jiang, Shuai Niu, Xing Zhang, Yun Zhang, Lu-Pan Yuan, Chuanxin He, Jin-Song Hu**

H. Luo, Prof. Chuanxin He

College of Chemistry and Environmental Engineering, Shenzhen University, Shenzhen, Guangdong 518060, P. R. China.
E-mail: hecx@szu.edu.cn

H. Luo, Dr. W. J. Jiang, S. Niu, Dr. X. Zhang, Dr. Y. Zhang, L. P. Yuan, Prof. J. S. Hu

Beijing National Laboratory for Molecular Science (BNLMS), CAS Key Laboratory of Molecular Nanostructure and Nanotechnology, Institute of Chemistry, Chinese Academy of Sciences (CAS), Beijing 100190, P. R. China.

E-mail: hujs@iccas.ac.cn

S. Niu, Dr. X. Zhang, L.P. Yuan, Prof. J.-S. Hu

University of Chinese Academy of Sciences, Beijing 100049, P. R. China.

Keywords: M-N-C, Oxygen reduction, Oxygen evolution, Nanostructures, Zn-air battery

Abstract:

Highly-efficient and stable bifunctional electrocatalysts for oxygen reduction and evolution is essential for aqueous rechargeable Zn-air batteries, which requires highly active sites as well as delicate structural design for increasing effective active sites and facilitating mass/electron transfer. Herein, we develop a scalable and facile self-catalyzed growth strategy to integrate highly active Co-N-C sites with three-dimensional (3D) brush-like nanostructure, achieving Co-N-C nanobrushes with Co, N-codoped carbon nanotube branches grown on Co, N-codoped nanoparticle assembled nanowire backbones. Systematic investigations suggest that nanobrushes delivered significantly improved electrocatalytic activity compared with nanowire or nanotube counterparts and the longer nanotube branches give the better performance. Benefiting from the increase of accessible highly active sites and enhanced mass transfer and electron transportation, the present Co-N-C nanobrush exhibits superior electrocatalytic activity and durability when used as bifunctional oxygen catalyst. It enables a rechargeable Zn-air battery a high peak power density of 246 mW cm^{-2} and excellent cycling stability. These results suggested that the reported synthetic strategy may open up possibilities for exploring efficient electrocatalysts for diverse applications.

1. Introduction

The rapid depletion of fossil fuels and increasing environmental concerns have stimulated the search for alternative energy conversion and storage devices.[1] Rechargeable Zn-air batteries have been considered as attractive alternatives in next-generation energy storage systems due to their high energy density, safety, and environmental friendliness.[2] The big challenge for this technique is the development of highly-efficient and stable air electrode. It requires highly active electrocatalysts for both oxygen reduction reactions (ORR) and oxygen evolution reactions (OER) to overcome sluggish kinetics for four electron transfer processes and significantly reduce the reaction overpotentials.[3] Although noble-metal based catalysts, such as platinum (Pt), ruthenium (Ru), iridium (Ir), and their alloys, are the best-known oxygen electrocatalysts, their commercialization are greatly hindered by their reserves, high cost, and still insufficient catalytic performance for bifunctional oxygen reactions.[4]

Over the past few years, much efforts have been devoted to developing non-noble metal bifunctional electrocatalysts, such as transition metal sulfide/oxides,[5] nitrides,[6] carbon materials[7] and so on[8]. Among these catalysts, the transitional metal-containing N-doped carbon materials (M-N-C, M=Fe, Co, Ni, etc.) have attracted intense attention. The transition metals in such catalysts greatly enhance the graphitization and thus electrical conductivity of carbon matrix, which provide them the better protection in turn from corrosion and aggregation during the electrochemical reactions.[4b, 9] Furthermore, the interactions and synergistic effects between metal species and N-doped carbon species enhance the intrinsic electrochemical activity for ORR and OER by electronically modulating the charge distribution on active sites and thus the adsorption/desorption of O_2 and intermediates.[4c, 10]

M-N-C materials are usually obtained from the direct pyrolysis of precursors, such as transition metal macrocycles/polymers (e.g. porphyrins, phthalocyanines) or the mixture of nitrogen-rich organic compounds and transition-metal salts, which commonly gives the inhomogeneous microstructures and uncontrollable agglomeration of active components due to the high reactivity of transition metal at high-temperature. Such structure could lead to the insufficient exposure of active sites as well as poor electron and mass transport.[11] One-dimensional (1D) nanostructures such as nanotubes,[12] nanofibers,[13] and nanorod[14] etc. were thus introduced to improve the electron transportation. The shortcoming is the insufficient surface area for accommodating accessible active sites.[5b] This could be improved by constructing secondary nanostructures on 1D scaffolds to form hierarchical three-dimensional (3D) structures.[15] The secondary nanostructures can not only significantly increase effective active sites but also improve mass transfer. Although some reports have demonstrated how to prepare hierarchical M-N-C materials via multi-step processing,[16] it is still necessary to exploit facile and scalable strategies to produce such 3D hierarchical M-N-C nanostructures.[15a, 17]

Herein, we developed a scalable facile strategy for fabricating 3D hierarchical Co-N-C brush-like nanostructures through self-catalyzed chemical vapor deposition. 1D Co-oxo framework nanowires with uniform distribution of N, C and Co at molecular level were used as precursors and backbones to produce N-doped carbon encased Co nanoparticles. N-doped carbon nanotubes was in-situ grown on the backbones catalyzed by themselves, forming Co-N-C nanobrush-like structures. This strategy could be extended to prepare Fe-based N-doped carbon analogues. To explore the unique role of such hierarchical nanobrush architecture, the nanoparticles-assembled backbones, nanobrushes with shorter branches, as well as Co-N-C nanotubes without 1D backbones were also prepared in

parallel for comparison. Systematic investigation revealed that the nanobrush architecture delivered the better mass transfer and electron transportation and the longer branches provided larger surface area thus the more active sites. As a result, it exhibited the significantly enhanced electrocatalytic activities for both ORR and OER, enabling a better rechargeable Zn-air battery with a power density up to 246 mW cm^{-2} and excellent cycling stability.

2. Results and Discussion

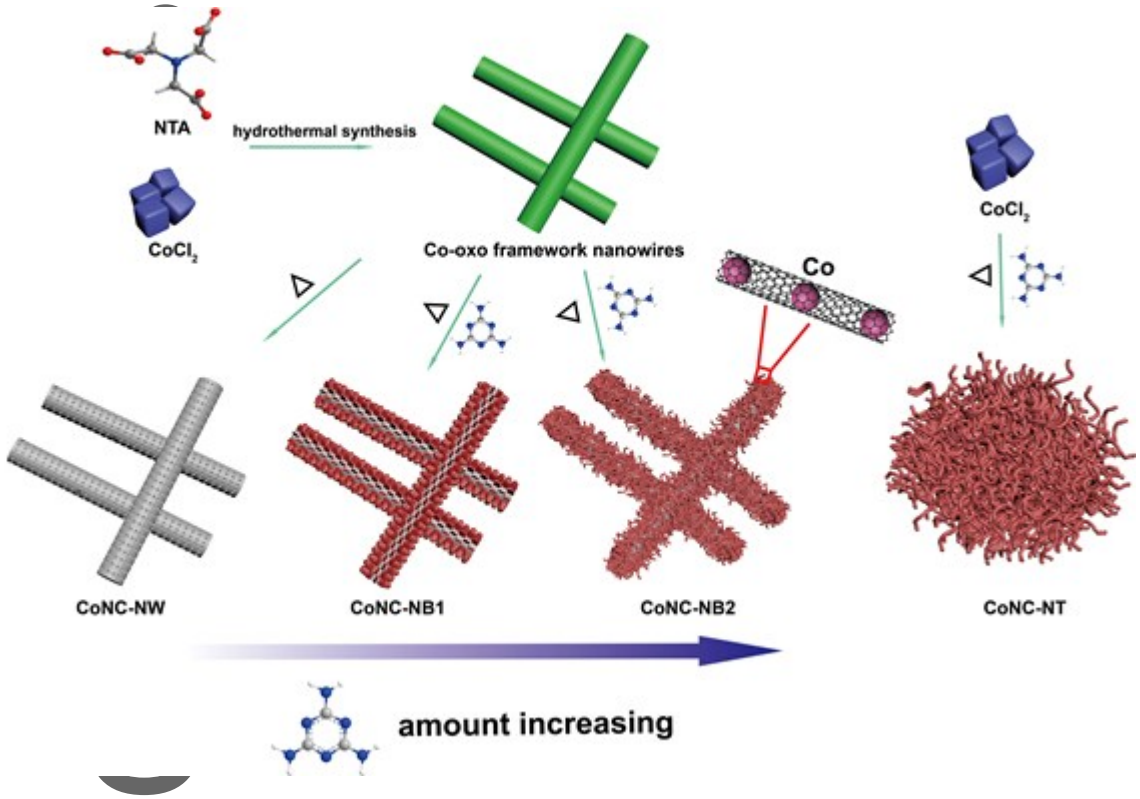

Scheme 1. Schematic illustration of the preparation of various Co-N-C nanostructures.

Various Co-N-C nanostructures were prepared by a two-step processing (see Experimental Methods for details). As shown in Scheme 1, 1D Co-oxo framework nanowires were first synthesized by hydrothermal treatment of the solution containing $CoCl_2$, NTA (Nitrilotriacetic acid), 2-propanol,

and water in a Teflon-lined stainless autoclave. As shown in Figure. S1 (EDS mapping), the 1D nanowire precursor was obtained with the uniform distribution of elemental Co, C, N, and O. X-ray photoelectron spectrum corroborates the presence of C, N, O, and Co (Figure. S2). Co-N-C catalysts with various morphologies were then prepared by varying the annealing process. If the precursor was directly pyrolyzed, the nanowire morphology remained (noted as CoNC-NW). If the precursor was pyrolyzed with the addition of melamine as the supplementary carbon and nitrogen source, the brush-like nanostructures were obtained by the growth of nanotube on CoNC-NW backbones self-catalyzed by the in-situ generated Co species (noted as CoNC-NB). The length of branches in CoNC-NB varied with the dosage of melamine. As a control, Co salt was directly pyrolyzed with melamine, giving irregular nanotubes (noted as CoNC-NT).

All these samples were first characterized by X-ray diffraction (XRD) technique. XRD patterns (Figure. S3) of CoNC-NT and CoNC-NW show clear diffraction peaks at 44.2^{o}, 51.5^{o} and 75.9^{o}, corresponding to cubic Co (JCPDS No.15-0806). For CoNC-NB samples, additional XRD peaks at 41.8^{o} and 47.6^{o} are observed, which can be assigned to hexagonal Co (JCPDS No.05-0727). These results indicate that metallic Co species exist in all samples. The XRD diffraction at 26.6^{o} for sample CoNC-NT and CoNC-NBs should be indexed to the graphitic carbon, consistent with the formation of carbon nanotubes.

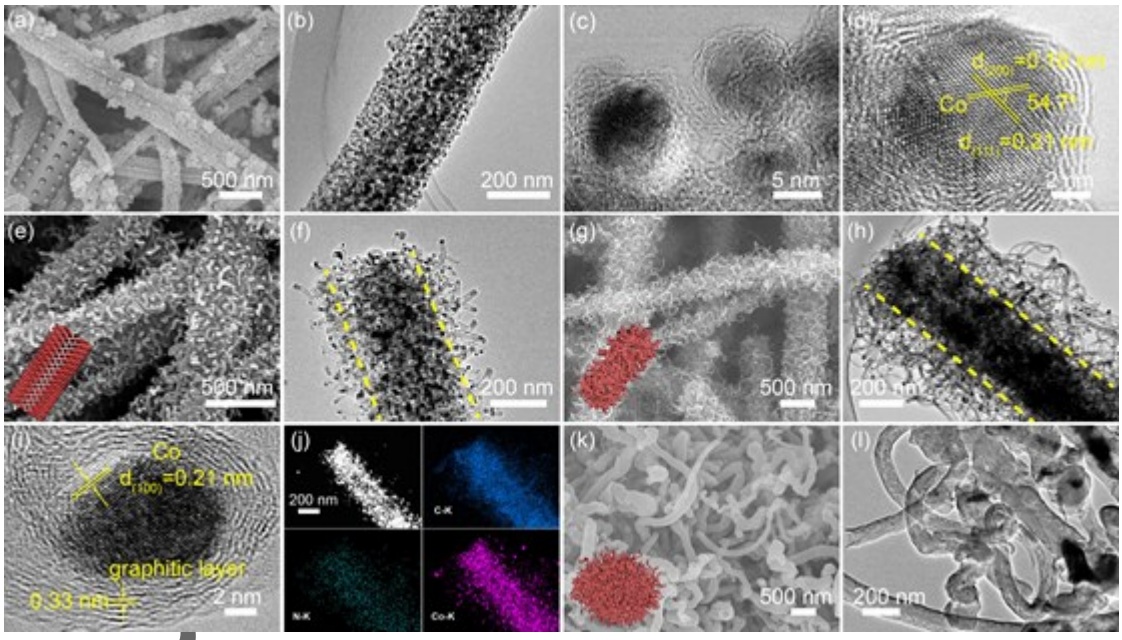

Figure. 1. (a-d) SEM and TEM images of CoNC-NW, (e, f) CoNC-NB1, (g-i) CoNC-NB2. (k, l) CoNC-NT. (j) EDS elemental mapping images of CoNC-NB2.

The morphologies of various CoNC catalysts were investigated by scanning electron microscope (SEM) and transmission electron microscope (TEM). As shown in Figure. 1a and 1b, CoNC-NW exhibits nanowire morphology with granular surfaces. TEM image indicates that the nanowire consists of a large number of nanoparticles in a homogeneous distribution. HRTEM image shows that these nanoparticles are in an average size of ~7 nm with carbon shells. The clear lattice fringes of 0.21 nm and 0.18 nm with an interplanar angle of 54.7^{o} correspond well to the (111) and (200) crystallographic planes of cubic Co (Figure. 1c and 1d), suggesting that these nanoparticles are Co. The elemental mapping results (Figure. S4) demonstrate the uniform distribution of C, Co, N, and O throughout the entire CoNC-NW, indicating the uniform N doping in the sample. For the sample CoNC-NB1 with the melamine dosage of is 20 : 1 (melamine : nanowire precursor), a large amount of nanotube branches with an average length of ~100 nm can be clearly observed on the entire

nanowire surface (Figure. 1e, 1f and S5). TEM image shows nanoparticles encapsulated at the end of nanotubes, suggesting the classic catalytic growth mechanism for these carbon nanotubes. Increasing the dosage of melamine to 40 : 1 leads to the longer nanotube branches in CoNC-NB2. The length can reach hundreds of nanometers (Figure. 1g and 1h). The typical features for carbon nanotubes can be clearly seen in the high-magnification TEM image (Figure. S6) and corroborated by the Raman spectrum of CoNC-NB2 (Figure. S7). HRTEM image taken on a single nanoparticle at the end of nanotube shows the lattice fringes in a spacing of 0.21 nm on the darker core (Figure. 1i). This agrees well with the (100) crystallographic planes of the hexagonal Co, indicating that the encapsulated nanoparticle is metallic Co. The lattice fringes in a spacing of 0.33 nm is the typical feature of graphitic carbon shells. The scanning TEM (STEM) and the energy-dispersive spectroscopic (EDS) elemental mapping (Figure. 1j) results evidence the homogenous distribution of C, N, and Co in the sample, implying the nature of N-doped carbon structures with Co species. Moreover, for the sample CoNC-NT, the irregular nanotube aggregation is observed in SEM and TEM images (Figure. 1k and 1l), which should be grown under the catalysis of Co species from the decomposition of Co salt.

The specific surface area and pore size distribution were further determined by N_2 adsorption-desorption experiments. The specific surface area of CoNC-NB2 is measured to be 194 $m^2 g^{-1}$, which is much higher than those of CoNC-NW (83 $m^2 g^{-1}$), and CoNC-NB1(133 $m^2 g^{-1}$), and CoNC-NT (42 $m^2 g^{-1}$) (Figure. 2a and S8). The pore volumes for these samples are 0.901, 0.676, 0.225, and 0.075 $cm^3 g^{-1}$ for CoNC-NB2, CoNC-NB1, CoNC-NW, and CoNC-NT, respectively (Figure. 2a). The pore distribution analysis on CoNC-NB2 shows three types of nanopores centered at about 0.5 nm, 3.8 nm, and 7.5 nm (Figure. S9). The micropores make active sites accessible at three-phase interfaces where ORR and OER take place. The mesopores would be beneficial for the mass transfer during electrochemical

reactions. These results indicate that the growth of nanotube branches and the increase of the length of nanotubes are effective for increasing the surface area and pore volume, thus increasing the number of accessible active sites in the catalysts. Compared with the disordered nanotubes in CoNC-NT, the 3D ordered hierarchical CoNC-NBs hold more accessible active sites, which will benefit O_2-involved electrochemical reactions.

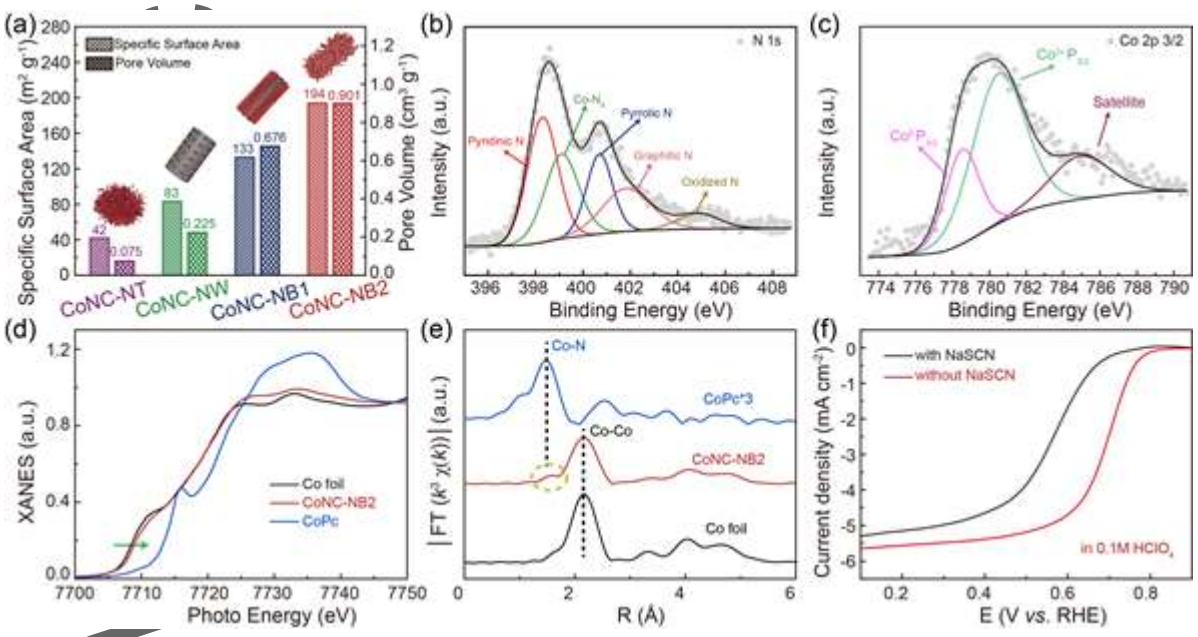

Figure. 2. (a) Specific surface area and pore volume of four samples. (b) N 1s and (c) Co 2p XPS spectra for CoNC-NB2. (d) Co K-edge XANES spectra and (e) EXAFS spectra in R-space for CoNC-NB2 as well as the reference Co foil and CoPc. (f) LSV curves of CoNC-NB2 in O_2-saturated 0.1M $HClO_4$ with or without 0.01M NaSCN.

X-ray photoelectron spectroscopy (XPS) measurements were further conducted on CoNC-NB2 to analyze the elemental compositions and chemical states. The signals of C, N, O, and Co agree with the EDS results (Figure. S10). The surface N content is measured to be 6.16 at.%, which is higher than 4.41 at.% for CoNC-NW (Figure S10). This high-level N doping should be from the N-rich precursor and melamine source. The high-resolution N 1s XPS spectrum can be deconvoluted into five main

peaks at 398.3eV, 399.1eV, 400.7eV, 401.8eV and 404.8eV, corresponding to pyridinic-N, Co-N_x, pyrrolic-N, graphitic N and oxidized-N, respectively (Figure. 2b).[18] The high-resolution Co $2p_{3/2}$ spectrum of CoNC-NB2 presents the signals of Co(0), Co(II), and satellite peaks (Figure. 2c).[3d, 19] Furthermore, the Co K-edge extended X-ray absorption near-edge structure (XANES) and fine structure (EXAFS) on CoNC-NB2 are analyzed to investigate its electronic structure and coordination environments using Co foil and CoPc as the references. It is found that the Co K-edge absorption edge position of CoNC-NB2 approaches that metallic Co with a slight shift to that of Co(II), suggesting that metallic Co is dominant in the sample and Co(II) possibly exists (Figure. 2d). In the Fourier-transformed (FT) k^3-weighted EXAFS spectra (Figure. 2e), the main peak at 2.3 Å corresponds to the metallic Co-Co scattering, corroborating metallic Co dominates in CoNC-NB2. The weak peak at 1.5 Å matches with Co-N coordination in reference to Co signal in CoPc. In order to clarify whether Co-N_x exists in CoNC-NB2, the conventional poisoning experiment was carried out using SCN^- ion to block the Co-N_x sites in catalyzing ORR.[20] Considering the instability of SCN^- ions in KOH solution, the ORR activity was measured in O_2-saturated 0.1 M $HClO_4$ with or without 0.01M NaSCN. It can be seen in Figure. 2f that the ORR activity of CoNC-NB2 decreases significantly in the presence of SCN^-. These results suggest that Co-N_x coordination sites should exist in CoNC-NB2 although its signal in EXAFS spectrum is suppressed by the dominant metallic Co.

The bifunctional electrocatalytic performance of the prepared samples was evaluated by measuring their ORR and OER activity. The representative cyclic voltammetric (CV) curves in N_2- and O_2-saturated 0.1 M KOH solution indicate that the CoNC-NB2 shows the apparent electrocatalytic ORR activity (Figure. S11). The linear sweep voltammetry (LSV) was further performed in O_2-saturated 0.1M KOH. All potentials are referred to reversible hydrogen electrode (RHE). As shown in

Figure. 3a, CoNC-NB2 shows the most positive onset potential (1.04 V) and the largest diffusion-limited current density (5.80 mA cm^{-2}) among all catalysts. The half-wave potential ($E_{1/2}$) of is calculated to be 0.88 V, better than Pt/C (0.85 V). This performance is also better than most of other state-of-the-art analogues (Table S1). The large diffusion-limited current density for CoNC-NB2 suggest the excellent mass transfer and electron transportation. CoNC-NB exhibits the half-wave potential and diffusion-limited current density similar to Pt/C and better than CoNC-NW and CoNC-NT. This implies that 3D hierarchical nanobrush structures benefit the ORR while the longer nanotube branches deliver the better performance due to the increased accessible active sites.

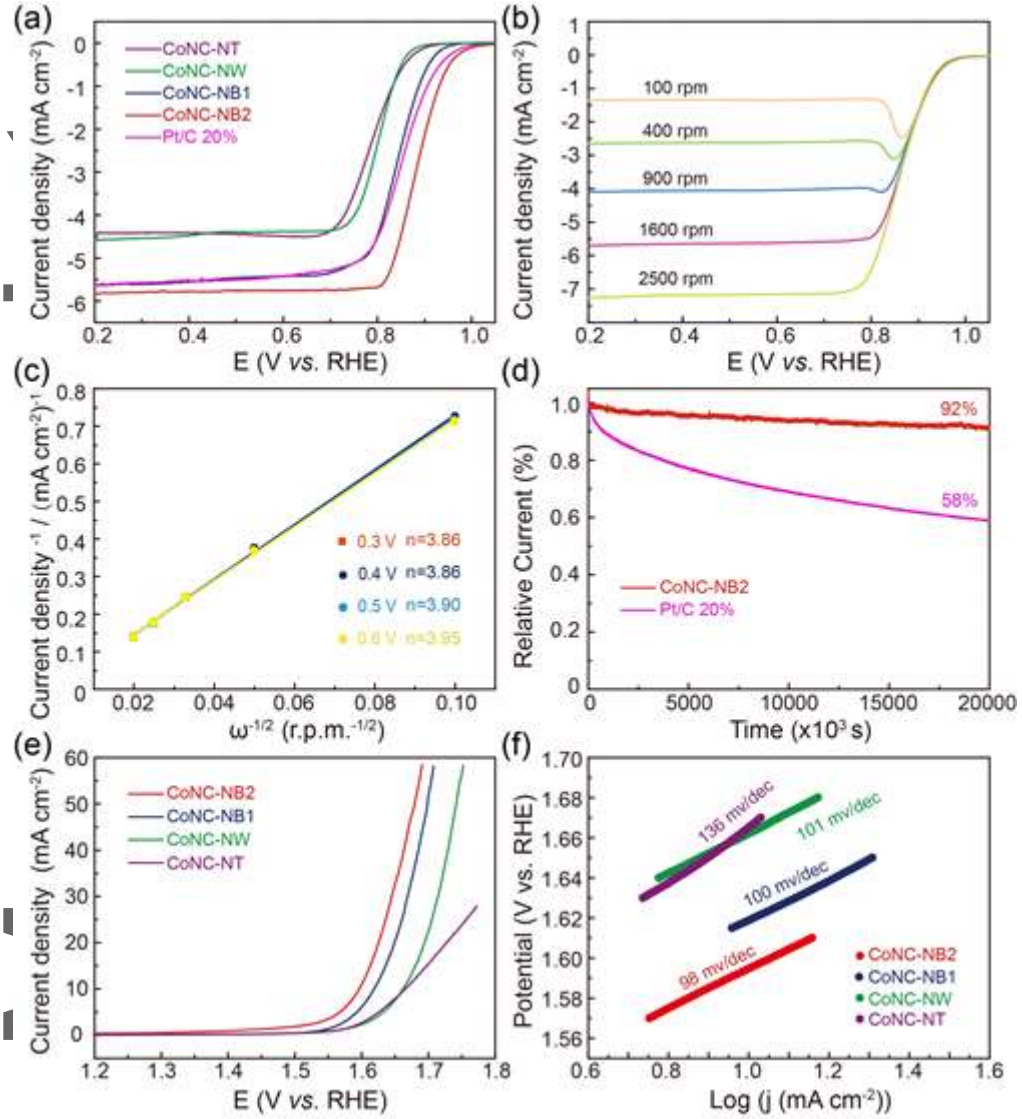

Figure. 3. (a) LSV curves of CoNC-NT, CoNC-NW, CoNC-NB1, CoNC-NB2, and Pt/C (20 wt% Pt), recorded at 1600 r.p.m. (b) LSV curves of CoNC-NB2 at various rotation speeds. (c) Corresponding K-L plots at various potentials and the caculated electron transfer numbers. (d) Chronoamperometric responses of CoNC-NB2 and Pt/C at 0.765 V. (e) LSV curves at a scanning rate of 5 mV s^{-1}, showing the OER activity of the catalysts. (f) Corresponding Tafel plots. ORR measurements are performed in O_2-saturated 0.1M KOH solution. OER measurements are performed in 1.0 M KOH solution.

To gain the insights into the reaction kinetics, the LSV curves of CoNC-NB2 are measured at different rotation rates (varying from 100 to 2500 rpm) in O_2-saturated 0.1M KOH solution and shown in Figure. 3b. The corresponding K-L plots (Figure. 3c) at different potentials (0.3-0.6 V) are subsequently obtained. All the K-L plots shows good linearity with a similar slope. The electron transfer numbers (n) are thus calculated at the potentials ranging from 0.3 V to 0.6 V. The values in the range of 3.86-3.95 indicate that ORR process on CoNC-NB2 follows an approximate four-electron pathway in a wide potential range. The long-term stability of CoNC-NB2 for ORR is then investigated by chronoamperometric technique and compared with Pt/C (Figure. 3d). It can be seen that the current density remains 87.5% after 20000 s continuous test for CoNC-NB2, whereas it drops to only 58% for Pt/C, suggesting that CoNC-NB2 exhibits a much better durability than Pt/C. The stability was further tested by CV cycling. As shown in Figure. S12, CoNC-NB2 displays almost unchanged LSV curve after 1000 CV cycles, corroborating its excellent stability for OER.

The electrochemical performances of various CoNC nanostructures for OER are further evaluated. As displayed in Figure. 3e, the CoNC-NB2 catalyst exhibits a polarization overpotential of 350 mV at a current density of 10 mA cm^{-2}, which is apparently smaller than that of CoNC-NB1, CoNC-NW and CoNC-NT catalysts. The Tafel slopes are derived from the LSV curves to evaluate the OER catalytic kinetics of these catalysts. As expected, CoNC-NB2 shows a smallest Tafel slope of 98 $mV{\cdot}dec^{-1}$, lower than that of CoNC-NB1 (100 $mV{\cdot}dec^{-1}$), CoNC-NW (101 $mV{\cdot}dec^{-1}$) and CoNC-NT (136 $mV{\cdot}dec^{-1}$). This implies the more favorable OER kinetics on CoNC-NB2 (Figure. 3f).

In addition, more control experiments were performed. To evaluate the influence of pyrolysis temperature on the catalyst morphology and performance, the control catalyst (CoNC-NB2-800) was synthesized using pyrolysis temperature of 800 ^{o}C versus to 700 ^{o}C for CoNC-NB2. LSV curves show

that CoNC-NB2-800 exhibits appreciably inferior ORR activity to CoNC-NB2 (Figure S13). SEM image (Figure S14) indicates that the 3D hierarchical nanostructure partly collapsed for CoNC-NB2-800, which should be responsible for the degraded ORR activity. This also suggest the importance of 3D hierarchical brush-like nanostructure in enhancing ORR performance. Moreover, CoNC-NB2 was treated in 0.5M H_2SO_4 at 80°C for 6h. As shown in Figure S15, the XRD pattern of acid-treated sample (CoNC-NB2-a) shows the clear diffraction signals from metallic Co, very similar to untreated CoNC-NB2. This result corroborates that the Co nanoparticles are encased in carbon nanotubes or carbon shells as shown in Figure 1. It also suggests that the present self-catalyzed growth strategy can provide transition metal-N-doped carbon catalysts stable in acidic media.

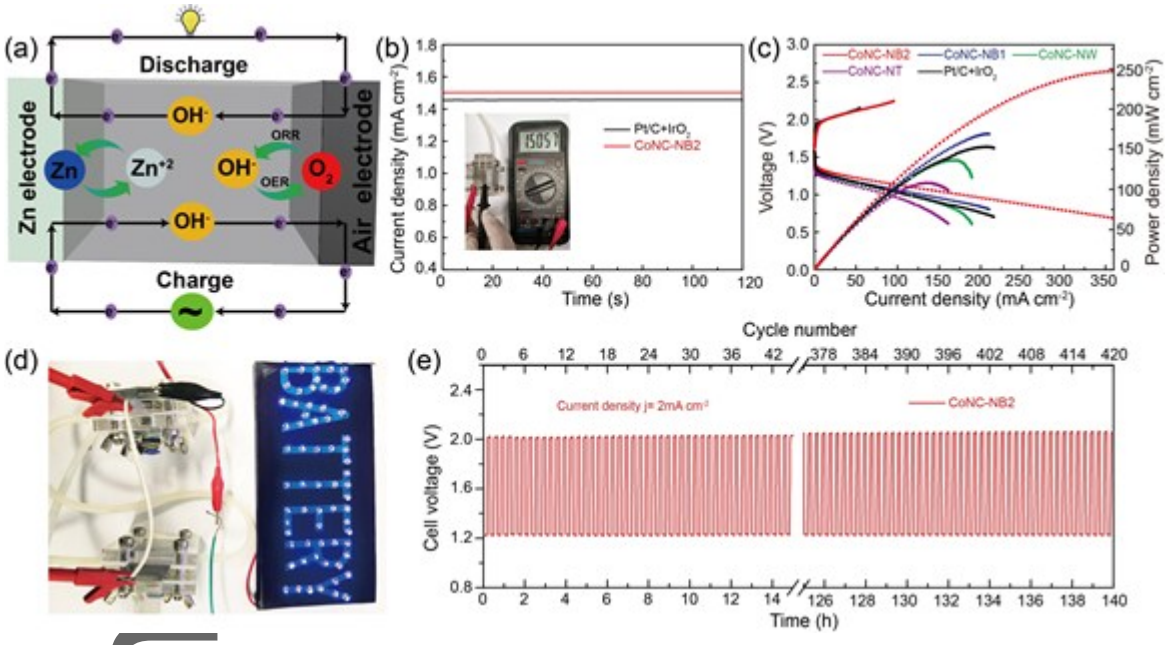

Figure. 4. (a) Scheme of the aqueous Zn-air battery. (b) Open-circuit voltage of the batteries based on CoNC-NB2 and Pt/C+IrO_2 cathodes (inset: direct voltage observation of the CoNC-NB2 based Zn-air battery). (c) Charge and discharge polarization curves and corresponding power density. (d) Optical image of the LEDs lighted by two CoNC-NB2 cathodes based Zn-air batteries connected in series. (e) Cycling stability of CoNC-NB2 cathode based Zn-air batteries at a discharge/charge current density of 2.0 mA cm^{-2}.

Considering the excellent activity and operational stability towards the reversible electrocatalysis of oxygen, CoNC-NB2 is evaluated as a bifunctional catalyst for air electrode in rechargeable Zn-air battery. Figure. 4a depicts a schematic aqueous Zn-air battery used in the present study, where a Zn plate is utilized as the anode and the catalysts deposited on carbon cloth is employed as the air cathode. A solution containing 6M KOH and 0.2 M zinc acetate is used as the electrolyte. The liquid rechargeable Zn-air battery employing CoNC-NB2 as the cathode shows a stable open-circuit voltage of 1.50 V (Figure. 4b), higher than that using Pt/C+IrO_2 catalyst as the cathode (1.47 V), suggesting its better performance. The polarization and power density curves of the Zn-air batteries using the above four CoNC catalysts and Pt/C+IrO_2 as control as well are plotted in Figure. 4c. It can be seen that the CoNC-NB2 catalyst exhibits a current density of ~350 mA cm^{-2} and a peak power density of ~246 mW cm^{-2}, much higher than those of other CoNC catalysts as well as Pt/C+IrO_2 catalyst (153 mW cm^{-2}). This performance is also better than most of other reported analogous materials (Table S2). As a demonstration, a device consisting of 65 LED lights can be easily powered by two Zn-air batteries with the CoNC-NB2 electrodes (Figure. 4d). The cycling performance of Zn-air battery with CoNC-NB2 as the air cathode was then examined. The charge/discharge current density is holding at 2.0 mA cm^{-2}. As shown in Figure. 4e, the initial discharge (1.22 V) and charge voltage (2.02 V) are maintained well during the cycling. Almost no voltage drop is observed after 140 h operation, indicating its good durability. These results indicate that the CoNC-NB2 catalyst can be a highly competitive alternative to the Pt/C+IrO_2 catalyst for further practical application in metal-air batteries. These results suggest that the 3D hierarchical nanobrush structure stands for a good platform for accommodating metal-nitrogen-carbon catalytic sites for their application in high-performance rechargeable Zn-air batteries.

Inspired by the simplicity and effectiveness of the present self-catalytic growth strategy, we extend it to prepare other transition metal-based nitrogen doped carbon analogues. For example, by using Fe salt instead of Co salt, we can easily obtain the similar Fe-oxo nanowire precursor (Figure. S16) and then FeNC materials with similar 3D hierarchical nanobrush-like architecture (Figure. S17). This FeNC nanobrushes also shows the better ORR activity than Pt/C in 0.1M KOH (Figure. S18). The results not only indicate that the developed method is versatile to some extent for preparing various nanostructures, but also suggests that the 3D hierarchical nanobrush structure is a good catalyst architecture for electrocatalytic applications by rendering more accessible catalytic sites as well as better mass transfer and electron transportation.

3. Conclusion

A scalable and facile self-catalyzed growth strategy has been developed to fabricate 3D hierarchical Co-N-C nanobrush. It consists of Co, N-codoped carbon nanotubes grown in situ on the surface of Co, N-codoped nanowire backbones derived from Co-oxo framework nanowires. The integration of longer carbon nanotube branches onto robust nanowire backbones provides the Co-N-C nanobrushes higher surface area for accommodating more accessible active sites and enhanced diffusion kinetics. As a result, Co-N-C nanobrush exhibits superior electrocatalytic activity and durability for both oxygen reduction and evolution reactions, enabling it as a promising bifunctional catalyst. The rechargeable Zn-air batteries with such Co-N-C nanobrush as air electrode delivers a high peak power density of 246 mW cm^{-2} and excellent cycling stability. The present synthetic strategy can also be applied to prepare Fe-based N-doped carbon analogues with 3D hierarchical nanobrush structure, opening up opportunities for rationally exploring hierarchically nanostructured electrocatalysts for high-performance energy devices.

4. Experimental Section

Materials: Nitrilotriacetic acid ($C_6H_9NO_6$), cobalt chloride ($CoCl_2$), iron chloride ($FeCl_2$), melamine ($C_3H_6N_6$), sodium sulfocyanate (NaSCN), perchloric acid ($HClO_4$), potassium hydroxide (KOH), zinc acetate ($Zn(CH_3COO)_2$), JM Pt/C (20 wt%), iridium dioxide (IrO_2), , 2-propanol, and absolute ethyl alcohol were purchased from Alfa Aesar in analytical grade (AR). Nafion (5%) was obtained from Sigma-Aldrich. All chemicals were used directly without further purification.

Synthesis of various M-N-C materials: In a typical synthesis, 6 mmol $CoCl_2$ was firstly dissolved in 30 mL deionized water. 3 mmol nitrilotriacetic acid and 10 mL 2-propanol were then added into the above solution. The solution was transferred into a Teflon-lined stainless autoclave for 6 h solvothermal reaction under 180^{o}C. The Co-oxo framework nanowires were subsequently obtained as the precursor. 50 mg obtained precursor and 2 g melamine were then separately placed in two ceramic boats in a tube furnace with melamine at the upstream side. The tube was heated to 700 ^{o}C under N_2 flow with a heating ramp of 6 ^{o}C min^{-1}. After cooling to room temperature, the black products were collected and marked as CoNC-NB2. If the dosage of melamine was decreased to 1 g, the product was noted as CoNC-NB1. If no melamine was used, the product was noted as CoNC-NW. If 6 mmol $CoCl_2$ was directly pyrolyzed with 2 g melamine under the same procedure, the product was noted as CoNC-NT. FeNC-NB2 was prepared using the same procedure, except for using $FeCl_2$ instead of $CoCl_2$.

Material characterizations: The morphologies of all samples were investigated by scanning electron microscope (SEM, S4800, Hitachi, Japan) and transmission electron microscope (TEM, JEM-2100F, JEOL, Japan) equipped with an EDS detector (Oxford Instrument, U.K.). X-ray diffraction (XRD) data were collected on a Rigaku D/Max-2500 diffractometer equipped with a Cu Kα1 radiation

(λ=1.54056Å, Regaku corporation, Tokyo, Japan). Raman spectra were measured on a Thermo Scientific DXR (laser wavelength: 532nm). X-ray photoelectron spectroscopic (XPS) spectra were recorded on a VG ESCALab220i-XL with a monochromic Mg Kα source. Nitrogen adsorption-desorption isotherms were measured on the Quadrasorb SI-MP at 77K. The specific surface area was calculated using the Brunauer-Emmett-Telle (BET) method. The pore size distribution curves were calculated by density functional theory (DFT) method. X-ray absorption near-edge spectroscopy (XANES) spectra of Co K-edges were acquired on the XAFS station of the 1W2B Beamline of the Beijing Synchrotron Radiation Facility (BSRF, Beijing). The fluorescence mode was used to record the X-ray absorption spectra of Fe K-edges. Data were collected using a Si (111) double crystal monochromator.

Electrochemical measurements: The electrocatalytic experiments were performed using a rotating ring-disk electrode (RRDE-3A, ALS, Japan) connected to an electrochemical workstation (CHI 760E, ChenHua, Shanghai, China) at room temperature. All ORR measurements were conducted with a standard three-electrode cell system consisting of a standard Ag/AgCl (saturated KCl solution) as the reference electrode, a graphite rod as the counter electrode, and a rotating ring disk electrode (RRDE, 4 mm in diameter) coated with each catalyst as the work electrode. OER test process is the same as that of ORR except using Hg/HgO (1M NaOH) as the reference electrode. Before the tests, RRDE was mechanically polished with 0.5-0.7 μm and then 0.03-0.05 μm alumina slurry to obtain a mirror-like surface, followed by washing with ethanol and dried in air. To prepare the working electrode, 3 mg catalyst was first dispersed in 600 μL ethanol under sonication for 15 min to form a homogeneous ink. 15.07 μL ink was then slowly loaded onto the clean surface of the RRDE and dried to achieve a catalyst loading of 0.6 mg·cm^{-2}. 2 μL Nafion (0.01 wt%) solution was later dropped onto

the electrode surface. After drying under ambient conditions, the electrode was ready for use. Commercial Johnson-Matthey Pt/C with 20 wt% Pt loading was used for comparison. Pt loading on electrode was 25.5 μg cm^{-2}.

The transfer electron number (n) was calculated by the Koutechy-Levich (K-L) equation:

$$\frac{1}{J} = \frac{1}{J_L} + \frac{1}{J_K} = \frac{1}{B\omega^{1/2}} + \frac{1}{J_K}$$

$$B = 0.62\, nFC_0(D_0)^{2/3}\nu^{-1/6}$$

Where J, J_K, and J_L are the measured current density, the kinetic density, and the diffusion limiting current density, respectively; ω is the rotation rate; ν is the kinetic viscosity of the electrolyte (0.01 $cm^2\ s^{-1}$ for 0.1 M KOH solution); F is the Faraday constant (F = 96485 C mol^{-1}); C_0 is the concentration of O_2 (1.2×10^{-3} mol L^{-1} for 0.1M KOH solution); and D_0 is the diffusion coefficient of O_2 (1.93×10^{-5} $cm^2\ s^{-1}$ for 0.1 M KOH).

Linear scanning voltammetry (LSV) for OER testing was executed with a rotation speed of 1600 rpm in the potential range from 0.2 to 1.0 V versus Hg/HgO at a scan rate of 5 mV s^{-1}. All polarization curves recorded without iR correction. All the potentials were converted to a RHE scale according to the following equation:

$$E_{RHE} = E_{Hg/HgO} + 0.059\ pH + 0.098$$

The home-made Zn-air battery was assembled with the as-prepared catalysts loaded on gas diffusion layer as air electrode, a Zn foil as metal electrode, and 6.0M KOH + 0.2M $Zn(CH_3COO)_2$ as electrolyte. Typically, CoNC-NB2 was dispersed in the isopropanol/5% Nafion solution with the catalyst concentration of 5mg mL^{-1}. The obtained catalyst ink was then drop-cast onto carbon paper

with a mass loading of 1 mg cm^{-2}. Mixed Pt/C + IrO_2 catalyst with the mass ratio of 1 : 1 was also used to replace CoNC-NB2 with the same loading on the carbon paper electrode to prepare the Zn-air battery. All Zn-air batteries were tested under the same experimental conditions.

Supporting Information

Supporting Information is available from the Wiley Online Library or from the author.

Acknowledgements

The authors acknowledge funding support from the National Key Research and Development Program of China (2016YFB0101202) and the National Natural Science Foundation of China (Nos. 21773263 and 21902162).

Received: ((will be filled in by the editorial staff))
Revised: ((will be filled in by the editorial staff))
Published online: ((will be filled in by the editorial staff))

References

[1] S. Chu, Y. Cui, N. Liu, *Nat. Mater.* **2016**, 16, 16.

[2] a) J. Zhang, Z. Zhao, Z. Xia, L. Dai, *Nat. Nanotech.* **2015**, 10, 444; b) J. Fu, Z. P. Cano, M. G. Park, A. Yu, M. Fowler, Z. Chen, *Adv. Mater.* **2017**, 29, 1604685; c) F. Meng, H. Zhong, D. Bao, J. Yan, X. Zhang, *J. Am. Chem. Soc.* **2016**, 138, 10226.

[3] a) Y. Li, H. Dai, *Chem. Soc. Rev.* **2014**, 43, 5257; b) C. Tang, B. Wang, H.-F. Wang, Q. Zhang, *Adv. Mater.* **2017**, 29, 1703185; c) Y. Tong, P. Chen, T. Zhou, K. Xu, W. Chu, C. Wu, Y. Xie, *Angew. Chem. Int. Ed.* **2017**, 56, 7121; d) Z. Yang, C. Zhao, Y. Qu, H. Zhou, F. Zhou, J. Wang, Y. Wu, Y. Li, *Adv. Mater.* **2019**, 31, 1808043.

[4] a) H. Luo, W.-J. Jiang, Y. Zhang, S. Niu, T. Tang, L.-B. Huang, Y.-Y. Chen, Z. Wei, J.-S. Hu, *Carbon* **2018**, 128, 97; b) X. Li, S. Zheng, L. Jin, Y. Li, P. Geng, H. Xue, H. Pang, Q. Xu, *Adv. Energy Mater.* **2018**, 8, 1800716; c) S. Liu, Z. Wang, S. Zhou, F. Yu, M. Yu, C.-Y. Chiang, W. Zhou, J. Zhao, J. Qiu, *Adv. Mater.* **2017**, 29, 1700874.

[5] a) Y. Li, C. Zhong, J. Liu, X. Zeng, S. Qu, X. Han, Y. Deng, W. Hu, J. Lu, *Adv. Mater.* **2018**, 30, 1703657; b) Q. Lu, J. Yu, X. Zou, K. Liao, P. Tan, W. Zhou, M. Ni, Z. Shao, *Adv. Funct. Mater.* **2019**, 29, 1904481; c) J.-Y. Wang, T. Ouyang, N. Li, T. Ma, Z.-Q. Liu, *Sci. Bull.* **2018**, 63, 1130; d) S. Zeng, X. Tong, S. Zhou, B. Lv, J. Qiao, Y. Song, M. Chen, J. Di, Q. Li, *Small* **2018**, 14, 1803409.

[6] a) Z. Cui, G. Fu, Y. Li, J. B. Goodenough, *Angew. Chem. Int. Ed.* **2017**, 56, 9901; b) G. Fu, Z. Cui, Y. Chen, Y. Li, Y. Tang, J. B. Goodenough, *Adv. Energy Mater.* **2017**, 7, 1601172; c) Q. Wang, L. Shang, R. Shi, X. Zhang, G. I. N. Waterhouse, L.-Z. Wu, C.-H. Tung, T. Zhang, *Nano Energy* **2017**, 40, 382.

[7] Y. Jia, L. Zhang, A. Du, G. Gao, J. Chen, X. Yan, C. L. Brown, X. Yao, *Adv. Mater.* **2016**, 28, 9532.

[8] a) J.-I. Jung, H. Y. Jeong, J.-S. Lee, M. G. Kim, J. Cho, *Angew. Chem. Int. Ed.* **2014**, 53, 4582; b) X. Han, X. Ling, D. Yu, D. Xie, L. Li, S. Peng, C. Zhong, N. Zhao, Y. Deng, W. Hu, *Adv. Mater.* **2019**, 31, 1905622; c) Q. Wang, L. Shang, R. Shi, X. Zhang, Y. Zhao, G. I. N. Waterhouse, L.-Z. Wu, C.-H. Tung, T. Zhang, *Adv. Energy Mater.* **2017**, 7.

[9] a) Y. Liu, H. Jiang, Y. Zhu, X. Yang, C. Li, *J. Mater. Chem. A* **2016**, 4, 1694; b) H. Luo, W.-J. Jiang, C. Lin, W. Dong, S. Niu, L.-B. Huang, X. Zhang, Z. Wei, J.-S. Hu, *Chem. Commun.* **2018**, 54, 8190.

[10] D. Deng, L. Yu, X. Chen, G. Wang, L. Jin, X. Pan, J. Deng, G. Sun, X. Bao, *Angew. Chem. Int. Ed.* **2013**, 52, 371.

[11] W. Ding, L. Li, K. Xiong, Y. Wang, W. Li, Y. Nie, S. Chen, X. Qi, Z. Wei, *J. Am. Chem. Soc.* **2015**, 137, 5414.

[12] Y. Nie, X. Xie, S. Chen, W. Ding, X. Qi, Y. Wang, J. Wang, W. Li, Z. Wei, M. Shao, *Electrochim. Acta* **2016**, 187, 153.

[13] Z.-Y. Wu, X.-X. Xu, B.-C. Hu, H.-W. Liang, Y. Lin, L.-F. Chen, S.-H. Yu, *Angew. Chem. Int. Ed.* **2015**, 54, 8179.

[14] L. Wan, J. Xiao, F. Xiao, S. Wang, *ACS Appl. Mater. Interfaces* **2014**, 6, 7735.

[15] a) Z. Pan, H. Chen, J. Yang, Y. Ma, Q. Zhang, Z. Kou, X. Ding, Y. Pang, L. Zhang, Q. Gu, C. Yan, J. Wang, *Adv. Sci.* **2019**, 6, 1900628; b) Z. Wang, J. Ang, J. Liu, X. Y. D. Ma, J. Kong, Y. Zhang, T. Yan, X. Lu, *Appl. Catal., B* **2020**, 263, 118344.

[16] a) P. Yu, L. Wang, F. Sun, Y. Xie, X. Liu, J. Ma, X. Wang, C. Tian, J. Li, H. Fu, *Adv. Mater.* **2019**, 31, 1901666; b) Y. Jiang, Y.-P. Deng, R. Liang, J. Fu, D. Luo, G. Liu, J. Li, Z. Zhang, Y. Hu, Z. Chen, *Adv. Energy Mater.* **2019**, 9, 1900911; c) J. Wu, L. Hu, N. Wang, Y. Li, D. Zhao, L. Li, X. Peng, Z. Cui, L.-J. Ma, Y. Tian, X. Wang, *Appl. Catal., B* **2019**, 254, 55.

[17] a) J. Pan, Y. Y. Xu, H. Yang, Z. Dong, H. Liu, B. Y. Xia, *Adv. Sci.* **2018**, 5, 1700691; b) Y. Qiao, P. Yuan, Y. Hu, J. Zhang, S. Mu, J. Zhou, H. Li, H. Xia, J. He, Q. Xu, *Adv. Mater.* **2018**, 30, 1804504.

[18] a) W. Li, W. Ding, Y. Nie, Q. He, J. Jiang, Z. Wei, *ACS Appl. Mater. Interfaces* **2019**, 11, 22290; b) W. Ding, Z. Wei, S. Chen, X. Qi, T. Yang, J. Hu, D. Wang, L.-J. Wan, S. F. Alvi, L. Li, *Angew. Chem. Int. Ed.* **2013**, 52, 11755.

[19] F. Sun, J. Wang, H. Chen, W. Li, W. Qiao, D. Long, L. Ling, *ACS Appl. Mater. Interfaces* **2013**, 5, 5630.

[20] Z. Li, L. Wei, W.-J. Jiang, Z. Hu, H. Luo, W. Zhao, T. Xu, W. Wu, M. Wu, J.-S. Hu, *Appl. Catal., B* **2019**, 251, 240.

3D hierarchical Co-N-C brush-like nanostructure was fabricated through a self-catalyzed chemical vapor deposition, which enables a rechargeable Zn-air batteries a high peak power density of 246 mW cm^{-2} and excellent cycling stability. The strategy also can be easily extended to prepare Fe-based M-N-C nanobrush analogues.

M-N-C, Oxygen reduction, Oxygen evolution, Nanostructures, Zn-air battery

Hao Luo, Wen-Jie Jiang, Shuai Niu, Xing Zhang, Yun Zhang, Lu-Pan Yuan, Chuanxin He,* Jin-Song Hu*

Self-Catalyzed Growth of Co-N-C Nanobrushes for Efficient Rechargeable Zn-Air Batteries

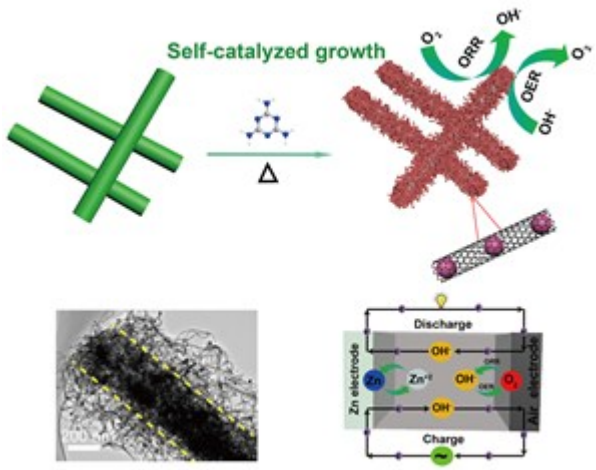

Author/s:
Luo, H;Jiang, W-J;Niu, S;Zhang, X;Zhang, Y;Yuan, L-P;He, C;Hu, J-S

Title:
Self-Catalyzed Growth of Co-N-C Nanobrushes for Efficient Rechargeable Zn-Air Batteries

Date:
2020-04-24

Citation:
Luo, H., Jiang, W. -J., Niu, S., Zhang, X., Zhang, Y., Yuan, L. -P., He, C. & Hu, J. -S. (2020). Self-Catalyzed Growth of Co-N-C Nanobrushes for Efficient Rechargeable Zn-Air Batteries. SMALL, 16 (20), https://doi.org/10.1002/smll.202001171.